



HAL
open science

Spheroidal graphite coalescence during thermal cycling in the ferritic domain of a high-silicon cast iron studied by optical microscopy and X-ray computed tomography

Mariana Alves Pegoraro, Christophe Tenailleau, André Ebel, Benoit Malard,
Jacques Lacaze

► To cite this version:

Mariana Alves Pegoraro, Christophe Tenailleau, André Ebel, Benoit Malard, Jacques Lacaze. Spheroidal graphite coalescence during thermal cycling in the ferritic domain of a high-silicon cast iron studied by optical microscopy and X-ray computed tomography. *Materials Today Communications*, 2020, 25, pp.101422. 10.1016/j.mtcomm.2020.101422 . hal-03165299

HAL Id: hal-03165299

<https://hal.science/hal-03165299>

Submitted on 10 Mar 2021

HAL is a multi-disciplinary open access archive for the deposit and dissemination of scientific research documents, whether they are published or not. The documents may come from teaching and research institutions in France or abroad, or from public or private research centers.

L'archive ouverte pluridisciplinaire **HAL**, est destinée au dépôt et à la diffusion de documents scientifiques de niveau recherche, publiés ou non, émanant des établissements d'enseignement et de recherche français ou étrangers, des laboratoires publics ou privés.



Open Archive Toulouse Archive Ouverte

OATAO is an open access repository that collects the work of Toulouse researchers and makes it freely available over the web where possible

This is an author's version published in:
<http://oatao.univ-toulouse.fr/26648>

Official URL

DOI : <https://doi.org/10.1016/j.mtcomm.2020.101422>

To cite this version: Pegoraro, Mariana Alves and Tenailleau, Christophe and Ebel, André and Malard, Benoit and Lacaze, Jacques *Spheroidal graphite coalescence during thermal cycling in the ferritic domain of a high-silicon cast iron studied by optical microscopy and X-ray computed tomography.* (2020) Materials Today Communications, 25. 101422. ISSN 23524928

Any correspondence concerning this service should be sent to the repository administrator: tech-oatao@listes-diff.inp-toulouse.fr

Spheroidal graphite coalescence during thermal cycling in the ferritic domain of a high-silicon cast iron studied by optical microscopy and X-ray computed tomography

Mariana Alves Pegoraro^a, Christophe Tenailleau^{a,*}, André Ebel^{a,b}, Benoit Malard^a, Jacques Lacaze^a

^a CIRIMAT, Université de Toulouse, CNRS, France

^b LCIS, Université de Bordeaux, France

ABSTRACT

Keywords:

Optical microscopy
X-ray computed tomography
Spheroidal graphite coalescence
High-silicon cast iron
Alloys
Materials characterization

High-silicon cast irons remain ferritic at higher temperature than usual cast irons and present both better oxidation resistance and higher mechanical strength. Such a high-silicon spheroidal graphite cast iron was heat treated up to 50 h in total at 800 °C in two different manners: under isothermal and cyclic conditions. Under the isothermal condition, the distribution of graphite inclusions did not vary significantly. On the contrary, temperature cycling led to spectacular coalescence whose evolution was observed after 1000, 2000 and 3000 cycles. Quite unexpectedly, the largest graphite particles - that were growing because of coalescence - showed an irregular outer surface after 1000 cycles, which evolved in impressive dendritic instabilities and then large protrusions after 2000 and 3000 cycles. Optical microscopy and X-ray computed tomography (XCT) were used to quantitatively study these microstructural changes.

1. Introduction

Cast irons are widely used in buildings (water pipes for instance), automotive (machines, engines and exhaust manifolds) and wind power (hubs) industries due to a combination of good casting properties and high mechanical properties. A graphitic cast iron is a composite material made of graphite precipitates within a Fe-rich matrix. It is primarily composed of iron, carbon and silicon, but other elements can be added to modify graphite shape and mechanical properties of the matrix. High silicon cast irons have been developed in the 1980's for automotive applications due to the increase of the upper temperature at which ferrite is stable [1]. Further, silicon improves oxidation resistance which is also an important property for parts included in propulsion systems [2]. For the last few years, high silicon grades have also been developed for other applications because of the intrinsic strengthening effect of this element on the material.

In the usual cast irons, graphite takes on a so-called lamellar shape. However, adding a small amount of magnesium and inoculating the melt leads to the formation of discrete graphite spheroids [3] with an associated marked increase in mechanical properties. Intermediate spheroidizing treatment may lead to various shapes of graphite known as compacted graphite with intermediate properties and better casting

soundness than spheroidal graphite irons (SGI) [4]. Control of the graphite particle shape is of utmost importance as this affects service properties, but is in practice difficult as this is sensitive to the casting conditions (cooling rate) and the presence of low-level of impurities [5].

This shape control is most generally carried out on 2D metallographic sections though 3D reconstructions have often given significant insight supporting better understanding of the microstructure formation in cast irons. It is worth mentioning here the patient work consisting in successive polishing of a 2D section until sufficient information can be gained to build 3D patterns. This allowed showing that cells of coral graphite [6] and compacted graphite [7] are both consisting of interconnected particles of graphite. Application of modern analytical means to cast irons started with the use of focused ion beam (FIB) milling by Velichko and Mücklich [8]. X-ray computed tomography (XCT) with a laboratory source [9] or with a synchrotron [10,11] allowed to perform a full reconstruction of large (mm size) compacted graphite cells. Also, the formation of spheroidal graphite during solidification could be followed on thin samples [12] and on mm size samples [13,14]. These above 3D works provided also quantitative information on the graphite size and shape distribution. Regarding SGI, more systematic studies have been carried out using laboratory XCT,

* Corresponding author.

E-mail address: tenailleau@chimie.ups-tlse.fr (C. Tenailleau).

e.g. to compare 3D size distributions as calculated from 2D observation and 3D measured distributions [15,16]. Yayun Yin et al. [17] investigated the effect of casting section size (cooling rate) on the 3D size and shape distribution of spheruloids.

The objective of this paper is to precisely document the possibilities offered by 3D investigations as they appear particularly suited to quantitatively describe spheroidal graphite overgrowths which have been recently evidenced after thermal cycling at 800 °C of high silicon cast irons [18]. It is worth stressing that it has been verified by differential thermal analysis that this maximum temperature is lower than the temperature for the start of the transformation of ferrite to austenite. The phenomenon investigated here thus proceeds without phase change but it could drive to a dramatic decrease in the mechanical properties depending on its actual 3D extension. When only 2D qualitative observations were reported in this preliminary work, both optical microscopy and XCT were used here to systematically quantify the microstructural variations. While the former technique is easily accessible and gives highly resolute sectional images down to a sub-micrometer scale, the latter is particularly useful to obtain a large number of sample layers in a non-destructive manner and to give detailed particle size, connection and shape distribution over the whole volume of analysis.

2. Experimental details

2.1. Materials preparation

The selected material was a high-silicon cast iron containing mainly 3.10 wt.% C and 4.45 wt.% Si, as well as 0.0037 wt.% Sb for avoiding degeneracy of spheroidal graphite during casting. It has been spheroidized and cast in Y-shape blocks as described previously [19]. For cycling treatment, ten samples ($20 \times 10 \times 2 \text{ mm}^3$) were machined out from the casting and a hole was drilled for hanging. They were then polished with a P1200 sand-paper, cleaned with acetone and alcohol and finally measured (in size and weight). Two other samples with $23 \times 15 \times 6 \text{ mm}^3$ in size were prepared from the same block and then polished and cleaned as the others. One of these latter samples, denoted as-cast in the following, will serve as a "reference" for microstructural studies. The second one was introduced in a Carbolite CWF 1300 resistance furnace heated to 800 °C and held for 50 h before being air cooled. This sample will be denoted as "isothermal".

For thermal cycling, a homemade facility was used which consists of a vertical resistance furnace and a samples carrier connected to a mechanical cylinder that moves the carrier from the lowest position in front of a fan to the highest position inside the furnace, and vice versa. The whole system, schematized in Fig. 1, is open to the air and computer controlled. The 10 samples were fixed to the sample holder with platinum wires and a thermocouple was spot-welded on one of them and linked to a computer allowing for real-time recording of the sample temperature.

The cycling procedure consisted in raising the samples inside the furnace and holding them inside until they spent approximately 60 s in the temperature range of 800 ± 10 °C. After this holding period, the sample holder was withdrawn from the vertical furnace and moved in front of a fan to accelerate cooling. The samples were kept in this lower position outside of the furnace until they reached 100 °C (a thermocouple was spot-welded on one of the samples and linked to a computer allowing to know when the temperature was reached), and were then raised again into the furnace for another cycle. The time slots required for heating and cooling were determined by preliminary tests. The process was repeated up to 3000 times, though interrupted every 200 cycles for weighing the samples so as to follow oxidation kinetics that will be presented elsewhere. Upon completion of 1000 cycles, three samples were taken out of the system and kept apart for analysis. This was repeated at 2000 cycles and after 3000 cycles the last three samples were withdrawn. Thus, at the end of 3000 cycles, three samples had

undergone 1000 cycles, three more 2000 cycles and three others had completed 3000 thermal cycles.

As three specimens were removed from the system after 1000 cycles and 2000 cycles, the holding time of the sample holder at the top position inside the furnace and at the bottom position in front of the fan were reduced in order to avoid temperature exceeding 810 °C upon heating. The resulting thermal cycles and the histogram of cumulated durations spent in the range 690–810 °C after 3000 cycles are presented in Fig. 2. Note that the time spent in the 800 °C ± 10 °C range after 3000 cycles actually reaches 56 h, which is the same order of magnitude as the duration of isothermal heat treatment.

2.2. Characterization methods

The five samples, i.e. the as-cast material, the isothermal sample and one sample from each cycling time, were then prepared for metallographic observations. A Secotom 50 Struers micro-chainsaw was used to make a vertical cut along each sample. They were then hot mounted and polished using SiC paper and diamond cloths. The samples were finally cleaned in an ultrasonic bath in ethanol before observation. 2D microstructural analysis was performed using an optical Zeiss AX10 microscope and image analyses were carried out with the ImageJ software. For the quantitative analysis, ten images were recorded in the central part of each sample that was observed to remain unaffected by decarburization and oxidation even after 3000 cycles. With this number of images, the total number of particles analyzed on each sample was in between 6800 and 8500. Note that particles with size less than or equal to 5 square pixels, i.e. less than about $2.5 \mu\text{m}^2$ in area at the magnification which was used, were not analyzed.

The same five samples were further cut to prepare a chip to be used for XCT analysis with a Phoenix/GE Nanotom 180 instrument from the French FERMAT FR3089 federation. These samples were polished to the shape of matches $\sim 0.7 \times 0.7 \times 10 \text{ mm}^3$ in size suitable for insertion in a 1 mm in diameter capillary used as sample holder for high resolution XCT. For XCT recording, the sample was located about 5 mm away from the source while the detector (Hamamatsu type C7942SK-05 with a resolution of 2300×2300 pixels) was positioned at 240–250 mm from the X-ray source. 1440 steps were used for a complete sample rotation and 5 images were summed up every 0.25° . Each image was recorded for 1 s. Typically, in these conditions, each scan lasts for about two and a half hours. A high voltage of 90 kV was used for the X-ray beam to fully pass through the sample. An intensity value of 100–150 μA , depending on the final sample size after polishing, was used for maximizing the phases peak shift on the grayscale histogram to enhance phase contrast. A voxel size of $1 \mu\text{m}^3$ was thus obtained. A few standard corrections included in the datos/x reconstruction program were then applied to the reconstructed volume, namely ring artefact reduction, geometry calibration and beam hardening correction. VGStudio max 2.1 program from Volume Graphic GmbH based in Germany was used for XCT analysis. With one acquisition for each sample, the total number of particles analyzed per sample was in between 3900 and 6300.

For 3D analysis, the images were systematically segmented using an automatic threshold value that was determined after computing the phase separation between the iron based matrix and the dark graphite particles, considering 1% reduction of the automatic threshold value (see Supplementary Information S1 for further details). Alike the case of Light microscopy, separation of graphite from porosity by XCT is not an easy task based on the similarity of their X-ray absorption coefficients and this was not attempted but particles as small as the voxel size could be determined.

Amongst the many parameters that have been proposed for 2D characterization of spheroidal graphite [20,21] we selected the shape factor or circularity, C, and the equivalent diameter, D_{2D} , which are defined as:

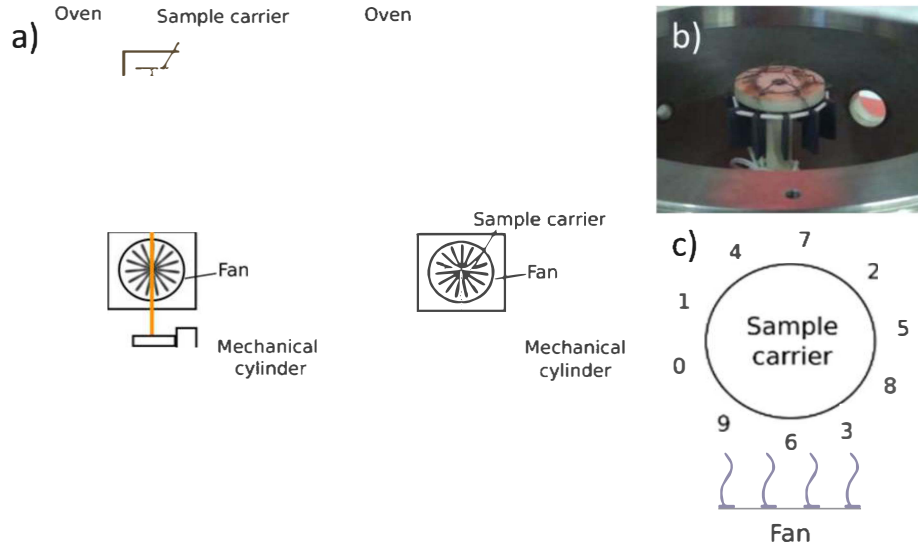


Fig. 1. a) Schematic of the vertical cyclic oxidation bench: samples carrier in the oven at the highest position (left) and in front of the fan at the lowest position (right); b) picture of the samples carrier at the lowest position; c) samples location on the samples carrier.

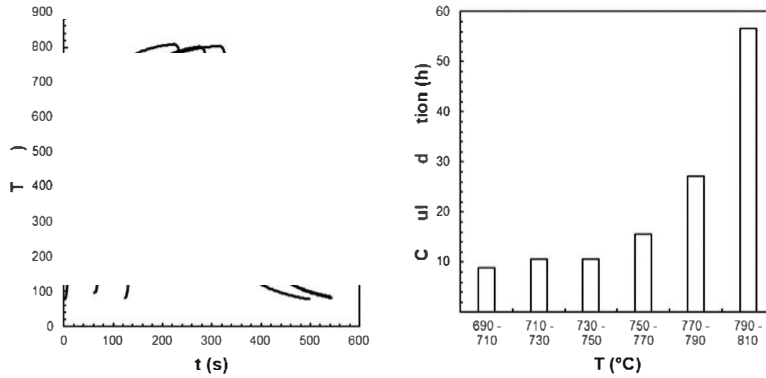


Fig. 2. Thermal cycles measured between 0 and 1000 cycles (marked as 1), 1000 and 2000 cycles (2) and between 2000 and 3000 cycles (3) (left). Histogram of the cumulated time spent in the range 690–810 °C after 3000 cycles taking into account the evolution of the thermal cycles (right).

$$C = 4 \cdot \pi \cdot \frac{S_{2D}}{P^2} \quad (1)$$

$$D_{2D} = 4 \cdot \frac{S_{2D}}{P} \quad (2)$$

in which S_{2D} and P are the area and the perimeter of the section of the particle.

Contrary to nodularity, which is defined to characterize a whole sample, circularity has the interest of being defined for each particle. Its drawback is that it includes at the same time information on the shape and roundness of the particles. The equivalent quantity in 3D is sphericity, Ψ , which is the most commonly used parameter [11,13,14,16]. It is defined as:

$$\Psi = \pi^{1/3} \cdot \frac{(6V)^{2/3}}{S_{3D}} \quad (3)$$

in which V and S_{3D} are the volume and the outer area of a particle. Both

C and Ψ would be equal to 1 for a perfect circle and sphere, respectively. For comparison purpose, the equivalent diameter of the particles resulting from the 3D image analysis, D_{3D} , is defined as:

$$D_{3D} = 6 \cdot \frac{V}{S_{3D}} \quad (4)$$

3. Results and discussion

Fig. 3 presents a micrograph for each of the five samples. The as-cast microstructure (Fig. 3a) is typical of a slightly hyper-eutectic SGI with large spheroids that deposited first and small nodules formed during the eutectic reaction. The sample obtained after isothermal treatment (Fig. 3b) shows only some limited coalescence of the graphite precipitates, with large spheroids that are rather larger than in the as-cast state. After 1000 cycles (Fig. 3c), the microstructure shows marked coalescence but it is also noticed that the large spheroids present now

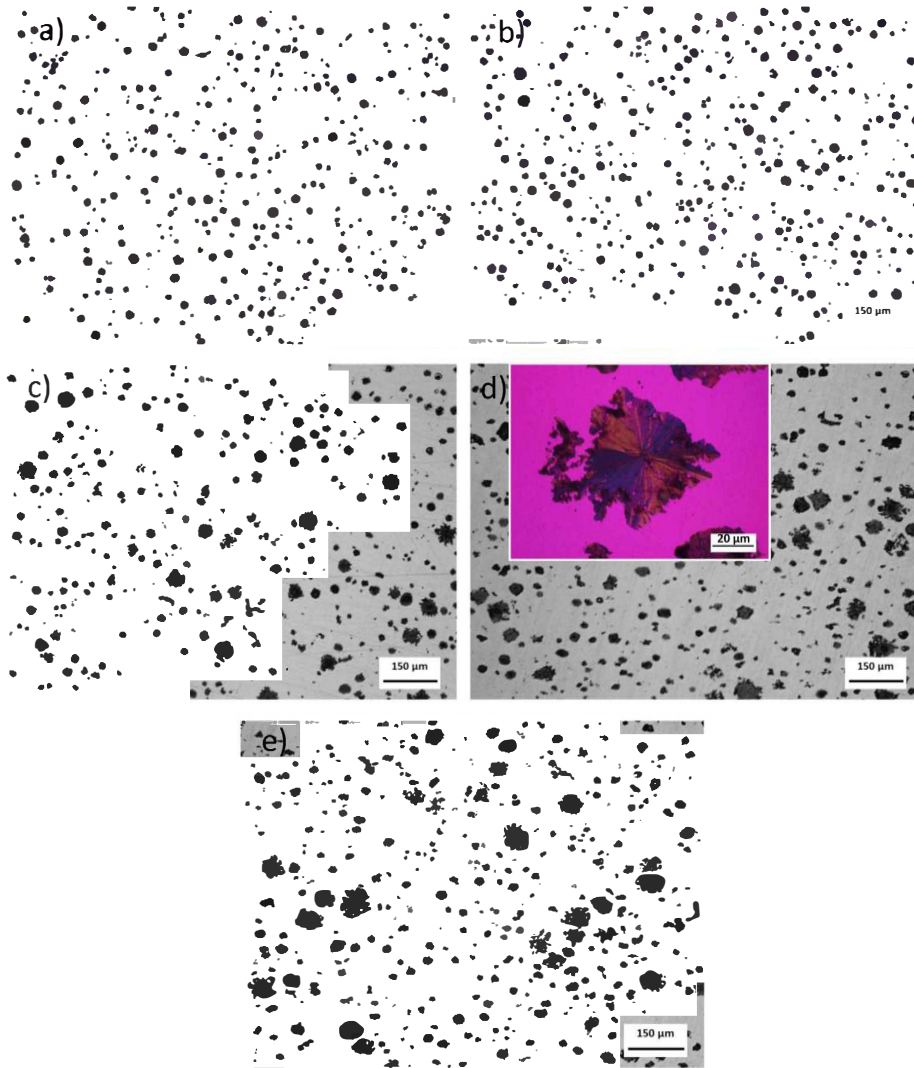


Fig. 3. Micrographs of the as-cast (a) and isothermally held (b) samples, as well as of samples after 1000 (c), 2000 (d) and 3000 thermal cycles (e). Insert in (d) shows dendritic overgrowths imaged under polarized light.

an irregular outer shape. After 2000 and 3000 cycles (Fig. 3d and e) the large spheroids have grown further and are even more irregularly shaped. The insert in Fig. 3d illustrates that many of the protuberances that developed around the large graphite precipitates are dendrite-like after 2000 cycles. This suggested that the carbon dissolved in the matrix during the holding at the maximum temperature of the thermal cycles re-precipitated upon cooling in only a few locations, eventually leading to these dendrites after a high enough number of cycles [18]. The micrograph in the insert of Fig. 3c was taken under polarized light which evidences that the dendritic protuberances were certainly twinned. Such a feature was observed on many of the protuberances of the 2000 sample and certainly explains the preferential growth along these definite directions. More detailed investigation could possibly relate the initial formation of the twins with the internal structure of the original

spheroids.

Growth of the largest precipitates during coalescence is expected to lead to the disappearance of the smallest precipitates. This was not evidenced with the observation of the microstructures in Fig. 3. For checking this, the area fraction of graphite was measured on the 2D section of all samples, giving the values (%) of 9.8(3), 11.0(1), 13.3(1), 15.1(2) and 16.3(3) for the as-cast, isothermal, 1000, 2000 and 3000 cycles samples, respectively, where the uncertainty on each last digit is given into brackets. Thus, this area fraction increases moderately with isothermal treatment but significantly with the number of cycles. This suggests that the coalescence process is accompanied by the formation of pores that cannot be distinguished from graphite with Light microscopy as further discussed later. Therefore, graphite particles denoted as such in the following might also be porosities.

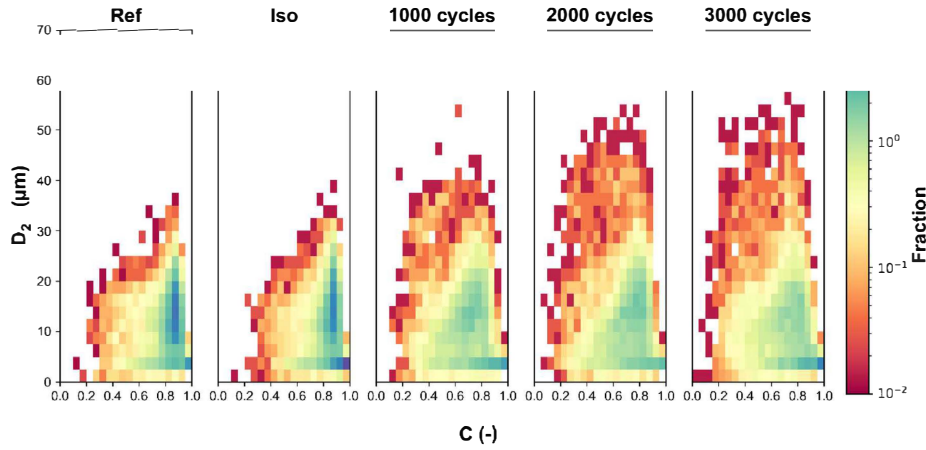


Fig. 4. Plots of particle equivalent diameter D_{2D} vs circularity C : comparison of as-cast sample (Ref) with the sample isothermally heat-treated sample (Iso) and with the samples cycled 1000, 2000 and 3000 times.

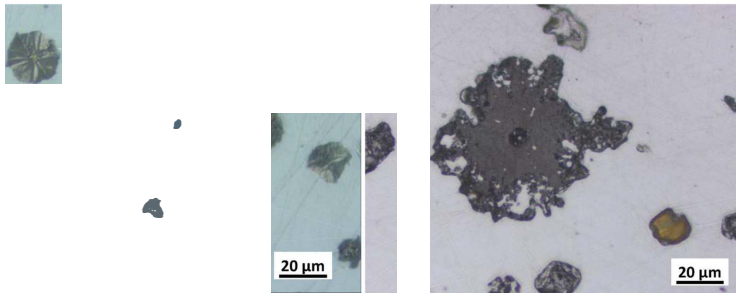


Fig. 5. Optical micrographs of the isothermal sample (left) and after 3000 cycles (right).

To quantify the change in graphite shape, the circularity of the particles was plotted as a function of the particles equivalent diameter D_{2D} . Fig. 4 compares the plots for the as-cast (Ref), isothermally heat-treated (Iso) and thermally cycled materials with a color scale that indicates the related number fraction. The plot for the as-cast material shows that most of the particles are quite round with a circularity higher than 0.7. Further, as expected from the observation of the microstructure in Fig. 3b, the distribution for the isothermally held sample shows very little difference with the as-cast material. A high magnification micrograph of this sample in Fig. 5a confirms that the contours of the graphite particles have remained smooth. After thermal cycling, the distributions are however significantly changed with the appearance of irregular large graphite precipitates which are larger and larger as the number of cycles increases. If it is considered that these are the largest particles in the reference material that have grown under cycling, i.e. those with $D_{2D} > 20 \mu\text{m}$, then it is interesting to note that the distribution of the remaining particles (green to blue in Fig. 4) does not change much. This is an indirect proof that small graphite particles that have been dissolved are replaced by pores keeping the size and shape of the original precipitates.

One feature of the graphs in Fig. 4 which is worth noticing is that the largest particles have circularity spanning an extended range from 0.2 to 0.8 when a significant shift to small values with the number of cycles would have been expected from Fig. 3. This first suggests that protuberances do not develop all around the large graphite particles but only in some definite directions. However, there is also a particular

feature of the growth process which is illustrated in Fig. 5b with a high magnification micrograph of a graphite precipitate after 3000 cycles. It is seen that while protuberances are still growing, they tend to merge with neighboring ones by means of graphite arches. These arches finally give a more overall rounded appearance to the particles that may explain the large range of circularity values measured on images acquired at lower magnification.

To complement the above 2D analysis, XCT was carried out on all five samples as illustrated in Fig. 6 which shows a 2D image extracted from the 3D record for each sample. As already detailed from 2D Light optical micrographs, the graphite particles in the as-cast and isothermal samples are mostly round. On the contrary, large graphite particles increase in size and become more irregular with thermal cycling. This evolution is exemplified in the inserts in Fig. 6a, b and e, where particles have been sorted according to their volume, from blue for the smallest ones to red for the largest ones. The particle in red in Fig. 6e is a clear example of how multiple protuberances in 2D are found interconnected when observed by XCT. Another example of interconnection is illustrated with the particle in yellow in Fig. 6c which further suggests that growth of the large graphite particles may lead to the merging of neighboring particles.

Alike the case of Light microscopy, separation of graphite from porosity by XCT is hardly possible because of the similarity of their X-ray absorption coefficients and was thus not attempted. Global measurements were first considered, namely the fraction of particles and their number. Fig. 7 shows the 2D area fraction and the 3D volume

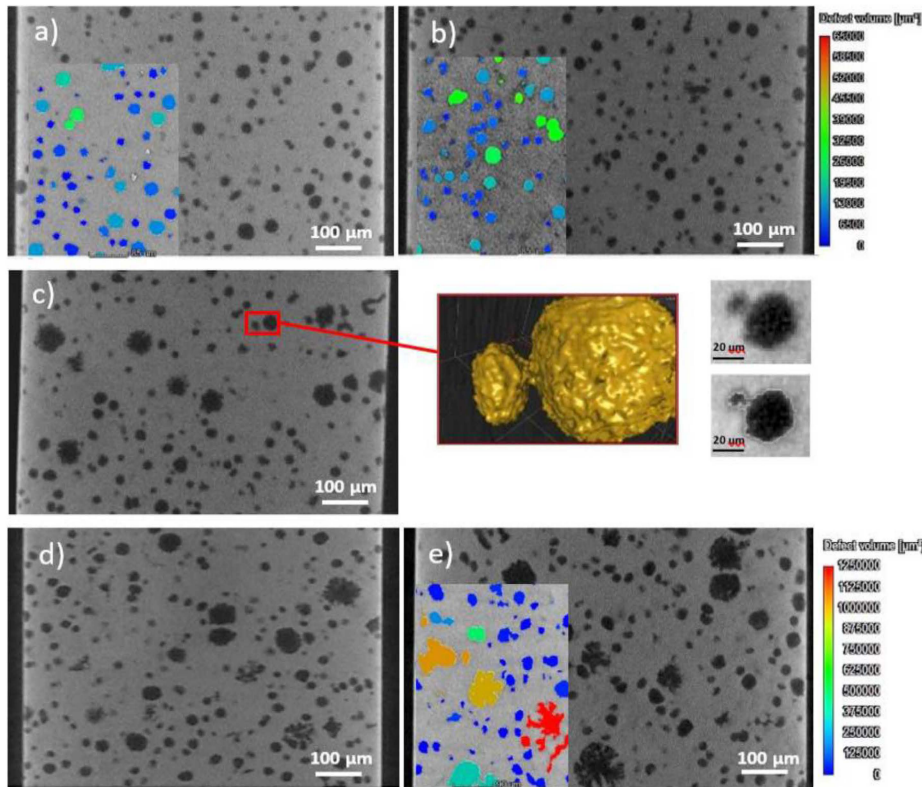


Fig. 6. 2D views for the as-cast sample in (a), the isothermally heat-treated sample (b) and the samples after 1000 (c), 2000 (d) and 3000 thermal cycles (e). An example of 3D interconnectivity is also materialized with a selected particle in (c). Renderings extracted from the 3D data are given for three of the samples, as illustrations.

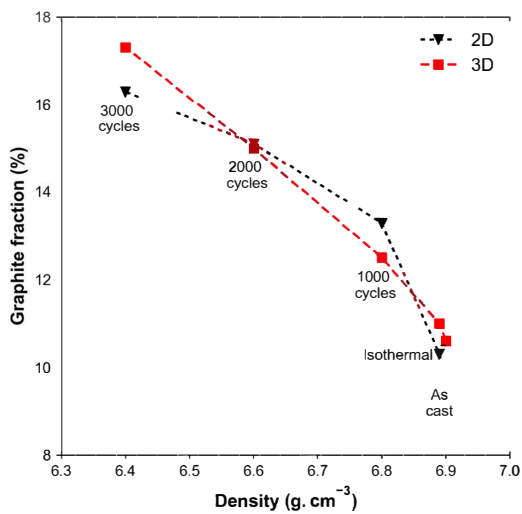


Fig. 7. Relation between 2D area and 3D volume fractions of graphite and the corresponding experimental density values for the reference and isothermal samples, and after 1000, 2000 and 3000 thermal cycles.

fraction of particles versus the density of the reference and cycled materials as measured on the XCT samples. There is a close relation between the density decrease and the increase in the area and volume fractions of particles. A simple mass balance demonstrates that the change in density corresponds perfectly to the change in the fraction of particles assuming that pores are formed at constant graphite fraction, see supplementary material S2. Concerning the evolution of the number of particles, it was noted that the 2D data did not show a smooth evolution as this was the case of the 3D counts. 3D counts are certainly much more significant and demonstrate an average of 10 % decrease of the number of particles every 1000 cycles.

To get some more detailed insight of the evolution of the particles, their distribution was obtained by sorting them with respect to their volume. The analysis was performed in a region of $\sim 0.5 \times 0.5 \times 0.5 \text{ mm}^3$ for each sample. 3D renderings are shown in supplementary material S3 while Fig. 8 presents the normalized size distributions. The upper limits of the first five classes used in Fig. 8 would correspond to an equivalent diameter D_{eq} of $\sim 20, 25, 31, 40$ and $50 \mu\text{m}$, respectively, if inclusions were spherical. It is impressive that the distributions are all quite similar. The only effect of coalescence because of cycling seen on this figure is a slight decrease of the relative number of particles in the smallest class and a corresponding increase in the two largest classes. Based on these observations, it seems that the largest particles engulf the smallest particles during cycling.

The actual possibility of such swallowing process is illustrated in Fig. 9 which presents superimposed micrographs as shown in Fig. 3a

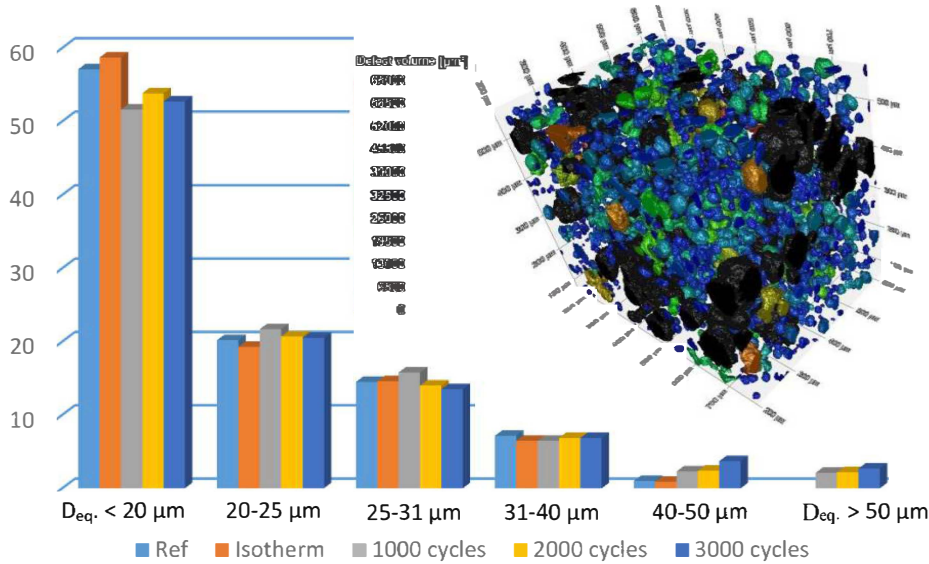


Fig. 8. Normalized count distribution of particles according to their volume V (or their equivalent diameter D_{eq} , such as $V = 4\pi/3(D_{eq}/2)^3$ when considering a sphere): $V < 4000 \mu\text{m}^3$ ($D_{eq} < 20 \mu\text{m}$), $4000 < V < 8000 \mu\text{m}^3$ ($20 < D_{eq} < 25 \mu\text{m}$), $8000 < V < 16,000 \mu\text{m}^3$ ($25 < D_{eq} < 31 \mu\text{m}$), $16,000 < V < 32,000 \mu\text{m}^3$ ($31 < D_{eq} < 40 \mu\text{m}$), $32,000 < V < 65,000 \mu\text{m}^3$ ($40 < D_{eq} < 50 \mu\text{m}$), and $V > 65,000 \mu\text{m}^3$ ($D_{eq} > 50 \mu\text{m}$). A 3D volume image obtained by XCT on a sample region of interest of $0.6 \times 0.44 \times 0.45 \text{ mm}^3$ after 3000 cycles is showing all different colored inclusion volumes (for instance, those bigger than $65,000 \mu\text{m}^3$ ($D_{eq} > 50 \mu\text{m}$) in black).

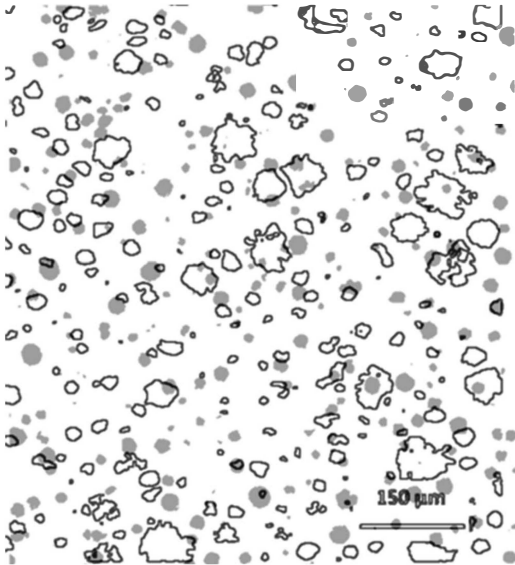


Fig. 9. Superimposition of a portion of the micrograph of Fig. 3a and of the particles contours of a portion of the micrograph of Fig. 3e.

and e. It is clearly seen that some of the graphite particles have become so large that their extension may encompass several of the initial precipitates. While the insert in Fig. 3c clearly showed that the protuberances grow along directions which are defined at their basis, it is quite evident that the carbon flux from neighboring graphite particles will

sustain a preferential growth of the protuberances towards them. This will support the merging mechanism and affects the irregularity of the shape of the growing graphite particles.

When comparing the circularity variations obtained from 2D metallographic observations with the sphericity variations based on XCT analysis, similar trends come out. Circularity evolves significantly during cycling with a dramatic decrease in particular for large particles. While more than 75 % of the graphite particles in the as-cast SGI are circular (circularity higher than 0.77), only about 40 % remain circular after thermal cycling whatever the number of cycles is (1000, 2000 or 3000 cycles). For the normalized distribution of sphericity, while a wider proportion of particles are a bit distorted from an ideal sphere in the as-cast state ($\sim 70\%$ of particles are in the 0.6–0.7 sphericity region) there is a strong loss of spherical shape upon thermal cycling associated with the growth of dendritic protuberances and a particle size increase (see also S4 and S5).

In order to stress the irregular shape of the particles, Fig. 10 shows the correlation between sphericity Ψ and particle equivalent diameter D_{3D} in the as-cast state, after isothermal holding and after 1000, 2000 and 3000 cycles. As was done in Fig. 4, the color code shows the normalized number fraction of precipitates. The reference and isothermal samples show again very similar distributions with sphericity ranging from 0.3 to 0.65. With cycling, this range extends slightly towards lower values, but the most significant change is the increase in size of the large particles and particularly those with lower sphericity. As for Fig. 4, it seems that the dense part of the distributions (colors green to blue) remains unchanged, being the same after cycling as in the as-cast sample. This suggests again that this part of the distribution comes from the small graphite particles that have dissolved during thermal cycling and gave pores.

One further thing should be mentioned regarding Fig. 10 which is that the maximum values of D_{3D} are about 35–40 μm when the maximum values of D_{2D} in Fig. 4 and those of the D_{eq} values in Fig. 8 were over 50 μm . This is due to the definition of the D_{3D} (Eq. 4) and shows

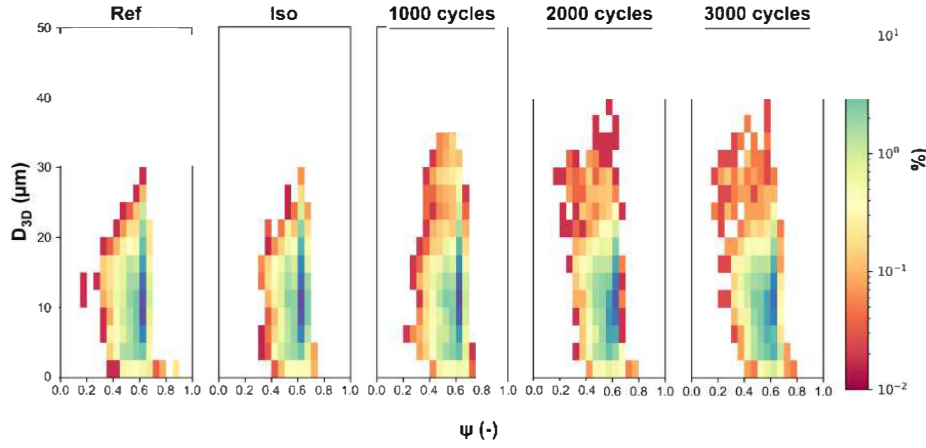


Fig. 10. Plots of sphericity Ψ versus particle equivalent diameter D_{3D} : comparison of as-cast sample (Ref) with the sample isothermally heat-treated sample (Iso) and the samples cycled 1000, 2000 and 3000 times.

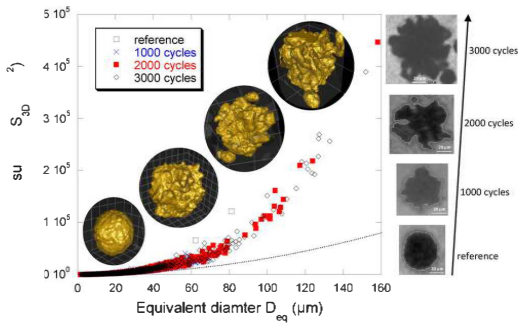


Fig. 11. Variation of the outer surface of the particles S_{3D} with the corresponding D_{eq} values for the reference and the three cycled samples. The dotted line represents the change of the surface of a perfect sphere. Examples of 3D and 2D images obtained by XCT. Scale bar is 20 μm for all 2D renderings.

that the S_{3D} values are much larger than for spheres of the same volume. In other words, the irregularity of the 3D outer shape of the large particles is much more pronounced than could be visualized with 2D images. This is evidenced by plotting the S_{3D} values as a function of the D_{eq} values for the reference sample and the three different cycled samples (Fig. 11). In this graph, thousands of points are superimposed at D_{eq} values less than 40 μm and are located close to the dotted line that represents the area S_{eq} of perfect spheres. At higher values of D_{eq} , the outer area of the graphite particles increases and dramatically diverges from the S_{eq} value. It is interesting to note that data for all three cycled samples strictly follow the same curve which is an evidence for a continuous coupled process of growth and coarsening all along the 3000 cycles. This process is illustrated with the 3D views of isolated particles and a 2D section extracted from the XCT data. One may note that the dendritic protuberances illustrated with Fig. 3 are smoothed due to the fact that XCT resolution is slightly lower than that of optical microscopy. Also, the merging of growing graphite particles with neighboring particles can be easily imagined with the largest particles shown in Fig. 11.

Finally, metallography analysis providing highly resolved images of particles but limited to a planar view, and XCT data showed that some particles can actually expand over a more complex shape in heat cycled cast iron materials. Isolated particles of particular dimensions can vary

depending on the shape they adopt after long thermal cycling, due to particle growths and/or aggregation phenomena. XCT technique was able to give a large distribution of graphite nodules in the cast volume and evidence for the complex (trans-)formation of inter-connected graphite nodules that will directly influence the mechanical properties of a material.

4. Conclusion

Heat treatment and harsh conditions can strongly influence the physical properties of materials. Visualizing sample cuts or full inner volumes and systematically analyzing their microstructural behavior by 2D microscopy and 2D/3D tomography are essential in better understanding and controlling their mechanical features, for instance.

Thermal cycling of a high-silicon cast iron leads to a marked coalescence of graphite particles in contrast with equivalent isothermal treatment. This coalescence is accompanied by a morphological instability of the largest particles that is characterized by the development of dendrite-like protuberances. Optical 2D analysis gave highly resolute sectional images down to a sub-micrometer scale of the materials and the 3D-XCT method was particularly useful to obtain a large number of sample layers in a non-destructive manner and to provide detailed particle sizes, connections and shape distributions over the whole volume of analysis. Hence, 2D and 3D analyses showed that, while an equivalent isothermal treatment keeps the initial shape of particles, more than a half of them lose their circularity and sphericity after 3000 thermal cycles. Volume analysis shows that some graphite nodules can then be three times bigger than at the beginning ($\sim 40 \mu\text{m}$ in diameter for the primary widest spheres) and the largest particles lose their initial spherical shape to evolve into larger and more complex precipitates. 2D and 3D images show spectacular coalescence associated with impressive dendritic instabilities over large graphite nodules. This detailed microstructural study evidences the unique transformation of large graphite nodules into overgrown particles that exhibit dendritic features. This microstructure instability is expected to appear for thermal cycles with peak temperature above 700 $^{\circ}\text{C}$. Such a microstructure evolution must be associated with a dramatic decrease of the mechanical properties of high-silicon cast irons which may explain why these alloys are not used above 700–720 $^{\circ}\text{C}$.

Declaration of Competing Interest

The authors declare that they have no known competing financial interests or personal relationships that could have appeared to influence the work reported in this paper.

Acknowledgments

Azterlan (Bizkaia) kindly provided the material used in this study.

Appendix A. Supplementary data

Supplementary material related to this article can be found, in the online version, at doi:<https://doi.org/10.1016/j.mtcomm.2020.101422>.

References

- [1] W. Fairhurst, K. Röhrig, High-silicon nodular irons, *Foundry Trade J.* 146 (1979) 657–681.
- [2] L. Delin, R. Logan, G. Burger, G. Liao, D. McFarlan, B. Black, R. Williams, High Silicon Cast Iron with Mixed Graphite (MG) Shapes for Elevated Temperature Applications, SAE technical paper 2007-01-12.
- [3] Classification and basic types of cast iron, *ASM Handbook Vol. 1A Cast Iron Science and Technology*, ASM Int., 2017, pp. 12–27.
- [4] M. Gorny, Cast iron: compacted graphite, *Encyclopedia of Iron, Steel and Their Alloys*, (2015), pp. 718–734.
- [5] J. Lacaze, D. Connetable, M. Castro Roman, Effects of impurities on graphite shape during solidification of spheroidal graphite cast irons, *Materialia* 8 (2019) 100471, <https://doi.org/10.1016/j.mtla.2019.100471>.
- [6] B. Lux, M. Grages, The spatial structure of graphite in pure Fe-C-Si alloys, *Pract. Metall.* 5 (1968) 123–126.
- [7] D. Stefanescu, L. Dinescu, S. Craciun, M. Popescu, Production of vermicular graphite cast-irons by operative control and correction of graphite shape, Translation from the Proceedings of the 1979 World Foundry Congress Appeared in *Fonderie* 397 (1980) 117–120.
- [8] A. Velichko, C. Holzapfel, F. Mücklich, 3D characterization of graphite morphologies in cast iron, *Adv. Eng. Mater.* 9 (2007) 39–45.
- [9] K. Salomonsson, A.E.W. Jarfors, *Trans. Tech. Pub., Zurich*, A. Diószegi, V.L. Diaconu, A.E.W. Jarfors (Eds.), Three-dimensional microstructural characterization of cast iron alloys for numerical analyses, 925 2018, pp. 427–435.
- [10] C. Chuang, D. Singh, P. Kenesei, J. Almer, J. Hryn, R. Huff, 3D quantitative analysis of graphite morphology in high strength cast iron by high-energy X-ray tomography, *Scripta Mater.* 106 (2015) 5–8.
- [11] C. Chuang, D. Singh, P. Kenesei, J. Almer, J. Hryn, R. Huff, Application of X-ray computed tomography for the characterization of graphite morphology in compact-graphite cast iron, *J. Miner. Mater. Charact. Eng.* 141 (2018) 442–449.
- [12] K. Yamane, H. Yasuda, et al., Influence of Mg on solidification of hypereutectic cast iron: X-ray radiography study, *Metall. Mater. Trans.* 46A (2015) 4937–4946.
- [13] M.K. Bjerre, In Situ Observations of Graphite Formation During Solidification of Cast Iron, PhD Thesis DTU mechanical engineering, 2017.
- [14] M.A. Azeem, M.K. Bjerre, R.C. Atwood, N. Tiedje, P.D. Lee, Synchrotron quantification of graphite nodule evolution during the solidification of cast iron, *Acta Mater.* 155 (2018) 393–401.
- [15] B. Mrzyglod, P. Matusiewicz, A. Tchorz, I. Olejarczyk-Wozenska, Quantitative analysis of ductile iron microstructure – a comparison of selected methods for assessment, *Arch. Foundry Eng.* 13 (2013) 59–63.
- [16] S. Lekakh, X. Zhang, et al., 3D characterization of structure and micro-porosity in two cast irons with spheroidal graphite, *J. Miner. Mater. Charact. Eng.* (2019).
- [17] Yajun Yin, Zhixin Tu, et al., 3D quantitative analysis of graphite morphology in ductile cast iron by X-ray microtomography, *Metall. Mater. Trans.* 48A (2017) 3794–3803.
- [18] A. Ebel, M. Alves Pegoraro, B. Malard, C. Tenailleau, J. Lacaze, Coarsening and dendritic instability of spheroidal graphite in high silicon cast iron under thermal cycling in the ferritic domain, *Scripta mater.* 178 (2020) 86–89, <https://doi.org/10.1016/j.scriptamat.2019.11.001>.
- [19] R. González-Martínez, U. de la Torre, J. Lacaze, J. Sertucha, Effects of high silicon contents on graphite morphology and room temperature mechanical properties of as-cast ferritic ductile cast irons. Part I – microstructure, *Mater. Sci. Eng. A* 712 (2018) 794–802.
- [20] Jianming Li, Man On Lai, Quantitative analysis of the irregularity of graphite nodules in cast iron, *J. Miner. Mater. Charact. Eng.* 45 (2000) 83–88.
- [21] B.I. Imasogie, U. Wendt, Characterization of graphite particle shape in spheroidal graphite iron using a computer-based image analyser, *J. Miner. Mater. Charact. Eng.* 3 (2004) 1–12.